

Trilinear-coupling-driven ferroelectricity in HfO₂Francesco Delodovici ¹, Paolo Barone ², and Silvia Picozzi¹¹Consiglio Nazionale delle Ricerche–SPIN, Università degli Studi “G. D’Annunzio,” I-66100 Chieti, Italy²Consiglio Nazionale delle Ricerche–SPIN, Area della Ricerca di Tor Vergata, Via del Fosso del Cavaliere 100, I-00133 Rome, Italy

(Received 25 March 2021; accepted 25 May 2021; published 9 June 2021)

Ferroelectricity in hafnia is often regarded as a breakthrough discovery in ferroelectrics, potentially able to revolutionize the whole field. Despite increasing interests, a deep and comprehensive understanding of the many factors driving ferroelectric stabilization is still lacking. We here address the phase transition in terms of a Landau-theory-based approach, by analyzing symmetry-allowed distortions connecting the high-symmetry paraelectric tetragonal phase to the low-symmetry polar orthorhombic phase. By means of first-principles simulations, we find that the Γ_{3-} polar mode is only weakly unstable, whereas the other two symmetry-allowed distortions, Y_{2+} and Y_{4-} (showing a nonpolar and antipolar behavior, respectively), are hard modes. While none of the modes, taken alone or combined with one other mode, is able to drive the transition, the key factor in stabilizing the ferroelectric phase is identified as the strong trilinear coupling among the three modes. Furthermore, the experimentally acknowledged importance of substrate-induced effects in the growth of HfO₂ ferroelectric thin films, along with the lack of a clear order parameter in the transition, suggested the extension of our analysis to strain effects. Our findings suggest a complex behavior of the Y_{2+} mode, which can become unstable under certain conditions (i.e., a tensile strain applied along the a direction), and an overall weakly unstable behavior for the Γ_{3-} polar mode for all the strain conditions. In any case, a robust result emerges from our analysis: independently of the different applied strain (be it compressive or tensile, applied along the a , b , or c orthorhombic axis), the need for a simultaneous excitation of the three coupled modes remains unaltered. Finally, when applied to mimic experimental growth conditions under strain, our analysis shows a further stabilization of the ferroelectric phase with respect to the unstrained case, in agreement with experimental findings.

DOI: [10.1103/PhysRevMaterials.5.064405](https://doi.org/10.1103/PhysRevMaterials.5.064405)

I. INTRODUCTION

Hafnium dioxide has been widely studied in its nonpolar phases as a high-dielectric-constant nontoxic oxide with crucial exploitation in microelectronics [1]. In fact, hafnia has been heavily employed as a gate dielectric in field-effect transistors, due to its compatibility with Si [2–4] and as a favorable gate dielectric in metal-oxide-semiconductor field-effect transistors. In 2011 the discovery of its ferroelectric phase in thin films [5,6] shed light on a new intriguing phenomenon and opened additional and promising avenues for HfO₂-based applications. In particular, due to their switchable persistent out-of-plane polarization, hafnia films could be used in high-speed nonvolatile memories and logic devices, such as ferroelectric field-effect transistors [7] and ferroelectric tunnel junctions [8]. Even though different polar phases have been detected [9–11], the polar orthorhombic phase $Pca2_1$ is mostly recognized to be responsible for ferroelectricity [5]. In bulk configuration, this phase is metastable at standard thermodynamical conditions, where the lowest-energy phase is the nonpolar monoclinic $P2_1c$ [5,12]; as such, the pristine ferroelectric phase cannot be stabilized through simple thermodynamical transformations. In fact, the Y-doped $Pca2_1$ phase has been recently obtained in bulk form through an ultrarapid cooling following high- T annealing [13]. On the other hand, when the thin-film limit is approached, the

orthorhombic polar phase appears to be energetically favored, becoming naturally competitive with the monoclinic nonpolar phase [14]. This condition is robust against the decrease of film thickness down to subnanometer scale [15,16], at variance with the usual behavior observed in perovskite-based thin films [17–20]. Indeed, as the film thickness decreases, the depolarization field produced by the incomplete screening of surface charges is expected to increase, challenging the stabilization of the out-of-plane switchable polarization. Nonetheless, stable ferroelectric HfO₂ nanometer-thick films with finite out-of-plane polarization are regularly grown on different substrates [10,21–23], a characteristic which further increases their potentiality in electronics. The mechanism causing the formation of the polar phase in films is probably dependent on the growth method, but evidences exist [5,21,24,25] revealing the tetragonal phase as possible precursor for the activation of ferroelectricity, as the transition temperature from the monoclinic phase is suppressed approaching low dimensions [24].

Despite the large amount of analysis, to the best of our knowledge, a clear microscopic description of the mechanism underlying the stabilization of ferroelectricity in hafnia is still missing. At a phenomenological level this mechanism is usually recognized as a superposition of different effects. Possible invoked causes are doping [26,27], oxygen vacancies [28], grain size, and film thickness [29]. Recently the scale-free

nature of ferroelectricity in hafnia and its high coercive field have been connected to intrinsic flat phonon bands [16].

Another important factor is represented by mechanical effects induced by the substrate [21,22,26,30]. In closer detail, the external strain plays a major role in the stabilization of the orthorhombic phase in Hafnia thin films, as induced by the lattice mismatch with the substrate. As confirmed by experiments [21] and simulations [14], strain changes the relative amount of competing phases present in the films, favoring either the polar orthorhombic or the nonpolar monoclinic phase depending on the lattice constant of the underlying substrate.

In this paper we present a first-principles-based study of the phase transition from the bulk nonpolar tetragonal $P4_2/nmc$ to the bulk polar orthorhombic phase $Pca2_1$ and interpret our results according to a symmetry-distortion mode analysis. We further include external strains applied to the HfO_2 primitive cell, in order to study the dependence of the distortion modes on external mechanical actions, with the aim of understanding how certain strain states may affect the phase transition. Finally, we address an experimentally relevant configuration as a benchmark of our analysis.

II. SYMMETRY MODE ANALYSIS

The transition from the high-symmetry nonpolar tetragonal phase ($P4_2/nmc$) to the polar orthorhombic phase ($Pca2_1$) couples atomic displacements with a nontrivial deformation of the cell. The analysis of the symmetry-allowed distortions [31–34] reveals five patterns connecting the two phases: three modes at the Brillouin zone center Γ_{1+} , Γ_{4+} , and Γ_{5-} , and two zone-boundary modes M_1 and M_3 . The Γ_{1+} involves atomic displacements coupled to a volume expansion, preserving the tetragonal symmetry. The Γ_{4+} mode is a pure-strain, volume-conserving mode responsible for lowering the tetragonal symmetry to the orthorhombic crystal class: it corresponds to a small distortion of the angle γ from its ideal tetragonal value to the low-symmetry relaxed value of 90.25° .

The full orthorhombic cell is obtained via the doubling of this resulting distorted tetragonal cell. In order to simplify the description, still retaining the main ingredients, we here focus only on the contributions to the phase transition given by atomic displacements, i.e., throughout our analysis we fixed the volume and shape of the cell to those of the orthorhombic primitive cell. In closer detail, this choice corresponds to freeze the Γ_{4+} and the normal-strain component of Γ_{1+} .

Since the atomic part of Γ_{1+} does not lower the symmetry of the atomic internal coordinates, one is allowed to freeze it at its maximum amplitude, taking the resulting $Ccce$ configuration (space group 68) as the high-symmetry structure for our analysis. We notice that *ab initio* calculations based on density functional theory reveal that the total energy of such idealized structure is 48 meV/f.u. higher than the energy of the tetragonal phase in its optimized volume; still, this difference is smaller than the energy separation between the tetragonal and the cubic phase (61 meV/f.u. above the tetragonal). Nonetheless, the choice of the high-symmetry parent structure in the orthorhombic class unveils some interesting features of the phase transition. The distortion-symmetry modes connecting the $Ccce$ to the $Pca2_1$ structure, reported in Fig. 1 labeled according to the $Ccce$ irreps, drive the system in three different

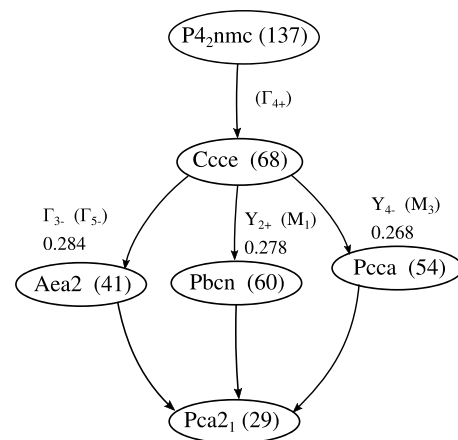


FIG. 1. The supergroup tree of the orthorhombic $Pca2_1$ structure. The parent structure $P4_2/nmc$ distorted into the $Pca2_1$ primitive cell is connected to the $Ccce$ phase through the action of the symmetry-lowering strain mode Γ_{4+} . The transformation to the $Ccce$ structure also involves a totally symmetric Γ_{1+} mode comprising both a strain and an atomic displacement. The space-group number of each structure is reported in parentheses. For each distortion, the amplitude of the maximum atomic displacement is reported in angstroms below the corresponding irreps. The displacements are intended from the $Ccce$ phase. The distortion modes are labeled according to the $Ccce$ ($P4_2/nmc$) irreps.

intermediate states, namely, the $Aea2_1$ (41), $Pbcn$ (60), and $Pcca$ (54), connected to the parent structure (68), respectively, through the modes Γ_{3-} , Y_{2+} , and Y_{4-} . We note that these three distortions correspond, respectively, to the Γ_{5-} , M_1 , and M_3 using the labeling of the tetragonal irreps. This can be verified by comparing the intermediate states produced by the activation of the single modes. Γ_{3-} is a polar mode, while Y_{2+} and Y_{4-} are nonpolar and antipolar modes, respectively, at the Brillouin-zone boundary.¹ The atomic displacement characteristic of each mode is reported in the lower half of Fig. 2. The oxygens rotate around the a primitive vector in the Y_{2+} mode whereas they undergo an antiphase shift parallel to the same axis a in the Y_{4-} . The overall effect of Γ_{3-} is to move apart the oxygens and the hafnium atoms along the c primitive vector, which causes the nonvanishing polarization.

Figure 2(a) reports the trend of the *ab initio* total energy as a function of a λ generalized coordinate representing the single mode distortion. We identify Y_{2+} and Y_{4-} as hard, stable modes and Γ_{3-} as a soft mode connected to a weak instability (4 meV/f.u.). Despite this small instability, the polar mode does not drive by itself the transition to the ferroelectric phase. Instead it leads towards the metastable $Aea2_1$ phase, which is 193 meV/f.u. higher in energy with respect to the $Pca2_1$. We thus analyze the *ab initio* total energies for the coupling between modes [reported in Fig. 2(b)]. The energy

¹The polar, nonpolar, and antipolar characters of the modes are determined by the symmetry properties of the corresponding irrep. A mode belonging to an irrep which possesses (does not possess) at least an axis that is left invariant under the point-group operations is said to be polar (nonpolar); if the polar irrep describes a zone-boundary mode, the corresponding distortion is said to be antipolar.

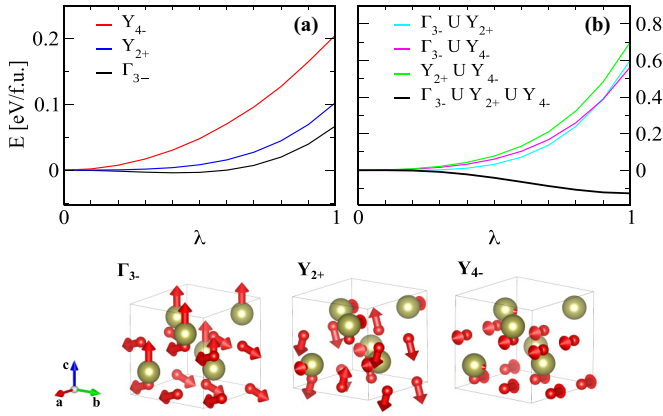


FIG. 2. Top: *Ab initio* energies (in eV/f.u.) of the single symmetry-distortion modes (a), along with their couplings (b), as a function of the generalized distortion coordinate λ . Each path consists of ten intermediate structures. The energy trend relative to the simultaneous excitation of the three modes is reported with a bold black line. Bottom: Atomic displacements of each single mode. Hafnium is colored in gold, and oxygen is colored in red. The arrows point in the direction of the displacement with a length proportional to its magnitude. For every mode the arrows relative to hafnium are magnified by a factor of 5.

trends reveal the stability of the *Ccce* structure against all pairwise combinations of modes; in other words, the hardness of both nonpolar modes suppresses the Γ_{3-} weak instability when combined to the polar mode. Additionally, the two-mode couplings strengthen the stability of *Ccce*, as can be seen by the difference in the energy scale between panel (a) and (b) in Fig. 2. The continuous black line in Fig. 2(b) corresponds to the trend of the three modes coupling. The

final structure at $\lambda = 1$ corresponds to an energy gain of 0.126 eV/f.u. and shows the *Pca21* symmetry group [35,36]. This confirms the necessity of the simultaneous excitation of the three modes to stabilize the ferroelectric phase, since the polar Γ_{3-} mode is unstable—neither by itself nor combined with a single hard mode—to provide the required energy gain. Even though symmetry analysis alone may not be sufficient, when multilinear couplings are at play, to identify the distortion mode responsible for the symmetry breaking (i.e., the primary order parameter in the language of Landau theory) [41], the possible role played by trilinear coupling in inducing ferroelectric transitions has been already highlighted in so-called hybrid improper ferroelectrics [37–40] and in Aurivillius ferroelectric compounds [42]. In most currently investigated hybrid improper ferroelectrics the transition is ascribed to the hybrid mode resulting from the coupling of two nonpolar distortions. On the other hand, the trilinear coupling that has been proposed to explain the anomalous ferroelectric transition in Aurivillius compounds occurs between individually hard modes, where the usual distinction between primary and secondary order parameters cannot be made [42]. Both these scenarios appear to be different from the situation realized in HfO_2 , that displays a soft polar Γ_{3-} mode (although leading to a weak instability) and a hybrid $Y_{2+} \cup Y_{4-}$ mode which is in fact the hardest one (see Fig. 2).

In order to gain more insights on the mode coupling driving the phase transition, we follow a Landau-theory approach and analyze the free-energy landscape surrounding the *Ccce* structure as a function of its symmetry-allowed distortion modes. The free energy expanded up to the sixth order in the order parameter describing each distortion and including all polynomial terms invariant under the symmetry operation of the high-symmetry space group [32] is

$$\begin{aligned}
 E(Q_{\Gamma_{3-}}, Q_{Y_{2+}}, Q_{Y_{4-}}) = & E_0 + \beta_{200} Q_{\Gamma_{3-}}^2 + \beta_{020} Q_{Y_{2+}}^2 + \beta_{002} Q_{Y_{4-}}^2 + \gamma_{111} Q_{\Gamma_{3-}} Q_{Y_{2+}} Q_{Y_{4-}} + \delta_{400} Q_{\Gamma_{3-}}^4 \\
 & + \delta_{040} Q_{Y_{2+}}^4 + \delta_{004} Q_{Y_{4-}}^4 + \delta_{220} Q_{\Gamma_{3-}}^2 Q_{Y_{2+}}^2 + \delta_{202} Q_{\Gamma_{3-}}^2 Q_{Y_{4-}}^2 + \delta_{022} Q_{Y_{2+}}^2 Q_{Y_{4-}}^2 \\
 & + \epsilon_{311} Q_{\Gamma_{3-}}^3 Q_{Y_{2+}} Q_{Y_{4-}} + \epsilon_{131} Q_{\Gamma_{3-}} Q_{Y_{2+}}^3 Q_{Y_{4-}} + \epsilon_{113} Q_{\Gamma_{3-}} Q_{Y_{2+}} Q_{Y_{4-}}^3 \\
 & + \eta_{600} Q_{\Gamma_{3-}}^6 + \eta_{060} Q_{Y_{2+}}^6 + \eta_{006} Q_{Y_{4-}}^6 + \eta_{420} Q_{\Gamma_{3-}}^4 Q_{Y_{2+}}^2 + \eta_{240} Q_{\Gamma_{3-}}^2 Q_{Y_{2+}}^4 \\
 & + \eta_{402} Q_{\Gamma_{3-}}^4 Q_{Y_{4-}}^2 + \eta_{204} Q_{\Gamma_{3-}}^2 Q_{Y_{4-}}^4 + \eta_{042} Q_{Y_{2+}}^2 Q_{Y_{4-}}^2 + \eta_{024} Q_{Y_{2+}}^2 Q_{Y_{4-}}^4 + \eta_{222} Q_{\Gamma_{3-}}^2 Q_{Y_{2+}}^2 Q_{Y_{4-}}^2 + \dots \quad (1)
 \end{aligned}$$

The order parameters $Q_{\Gamma_{3-}}$, $Q_{Y_{2+}}$, and $Q_{Y_{4-}}$ represent the amplitude (dimensionless) of the three modes. β , γ , δ , ϵ , η are the expansion coefficients (in eV/f.u.). The condition $Q = (Q_{\Gamma_{3-}}, Q_{Y_{2+}}, Q_{Y_{4-}}) = (0, 0, 0)$ corresponds to the high-symmetry *Ccce*, whereas $Q = (1, 1, 1)$ corresponds to the orthorhombic *Pca21*. The free energy includes coupling at different orders: trilinear γ , biquadratic δ , and some more complex term, i.e., bilinear-cubic ϵ and quadratic-quartic η . The odd terms in Eq. (1), the trilinear and the bilinear-cubic terms, prevent the degeneracy of the *Pca21* against the simultaneous inversion of each mode: thus the phases $Q = (-1, -1, -1)$ and $(1, 1, 1)$ are not energetically equivalent. Instead, the *Pca21* is fourfold degenerate in total energy against the simultaneous inversion of couples of modes. Indeed the phases

$Q = (1, 1, 1)$, $(1, -1, -1)$, $(-1, 1, -1)$, and $(-1, -1, 1)$ are all energetically equivalent. This multiplicity is consistent with the index of the group-subgroup relation between the high-symmetry *P42/nmc* (crystallographic point group D_{4h} of order 16) and the low-symmetry *Pca21* (crystallographic point group C_{2v} of order 4) space groups, that provides the number of allowed domains in any ferroic phase transition [43]. It could also be connected to the number of equivalent hafnia growth domains detected in some experimental configurations; see, e.g., the heterostructure considered in Sec. III B, where four equivalent growth orientations are identified [22]. Furthermore, the trilinear terms set the polarity of the pseudorotations combination against an inversion of the path: $Y_{2+} \cup Y_{4-}$ must have the same parity of the

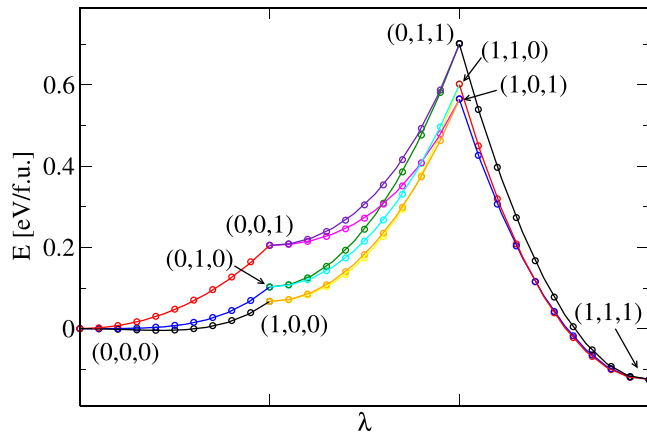


FIG. 3. Fit of *ab initio* energies, represented by colored dots, with the free energy expressed in Eq. (1) for the zero-strain case. The path connects the high-symmetry structures from the *Ccce* to the *Pca2*₁. The figure shows only part of the energy landscape, i.e., it reports only some portions of the fit: two-mode and three-mode combinations are not shown. Each high-symmetry structure is labeled with the values of the vector $(Q_{\Gamma_{3-}}, Q_{Y_{2+}}, Q_{Y_{4-}})$, thus $(0, 0, 0)$ corresponds to the *Ccce* and $(1, 1, 1)$ corresponds to the *Pca2*₁.

Γ_{3-} mode, which means that the coupling of the rotations corresponds to a polar distortion, as it happens in hybrid improper ferroelectrics [37–40], with the crucial difference that such hybrid polar mode does not soften in HfO_2 . Additionally, the decomposition of the polarization onto the different modes reveals the dominating contribution of Γ_{3-} , with the hybrid polar mode $Y_{2+} \cup Y_{4-}$ only providing a small, higher-order correction.

Based on these considerations we focus on the patterns connecting $Q = (0, 0, 0)$ to $Q = (1, 1, 1)$ via the high-symmetry structures produced by the three single modes and their couplings. Each portion of the path consists of ten intermediate structures. In practice, we first computed the *ab initio* total energies of different structures along these paths. We then extracted a numerical estimate of the Landau coefficients through a fit of the total energies with the polynomial in Eq. (1). From the ratio of the coefficients we deduced the terms leading the transition and the character of the different contributions to the free energy. Figure 3 reports the *ab initio* energies and the relative fit for the case where no strain is applied. The initial portion of the path coincides with the trends in Fig. 2(a). The two pseudorotations increase the energy of *Ccce* in a range of 0.1–0.2 eV/f.u. with a monotonous trend: this behavior is captured by the positiveness of β_{020} , β_{002} and δ_{040} , δ_{004} . Interestingly, among all the parameters, the trilinear coupling is by far the dominant term: $\gamma_{111} \approx -1.08$ eV/f.u., confirming that the three distortions are all equally necessary to complete the phase transition when no strain is present. We further note that the coefficients of the polar mode β_{200} and δ_{200} have opposite signs, reflecting the instability of the Γ_{3-} mode, evaluated as 3.9 meV/f.u.. It should be stressed that $\beta_{020} \approx 1$ meV/f.u. is remarkably smaller than all the other parameters as can be seen in Table I. This is interesting since a change in the sign of this parameter corresponds to the insurgence of an instability in Y_{2+} . This may occur by means

TABLE I. Fit coefficients obtained by interpolation of the *ab initio* total energies with Eq. (1) for the case of zero-applied strain.

Coefficient	Value (eV/f.u.)	Coefficient	Value (eV/f.u.)
$\beta_{(200)}$	−0.046	$\epsilon_{(311)}$	−0.147
$\beta_{(020)}$	0.001	$\epsilon_{(131)}$	−0.372
$\beta_{(002)}$	0.18	$\epsilon_{(113)}$	−0.238
$\gamma_{(111)}$	−1.08	$\eta_{(600)}$	−0.011
$\delta_{(400)}$	0.124	$\eta_{(060)}$	−0.01
$\delta_{(040)}$	0.111	$\eta_{(006)}$	−0.005
$\delta_{(004)}$	0.029	$\eta_{(420)}$	−0.05
$\delta_{(220)}$	0.444	$\eta_{(402)}$	0.007
$\delta_{(202)}$	0.264	$\eta_{(240)}$	0.036
$\delta_{(022)}$	0.355	$\eta_{(042)}$	0.026
		$\eta_{(024)}$	0.012
		$\eta_{(204)}$	0.021
		$\eta_{(222)}$	0.222

of some external perturbation, e.g., mechanical strain, which modifies the relative stability of the atomic configurations along the distortion path. Despite the corresponding sixth-order η being negative, they are significantly smaller than the δ , thus they do not alter the stable character of the rotations. Nonetheless, such terms are necessary to obtain a qualitatively reliable fit. We further verified that the inclusion of seventh- and eighth-order terms in the free-energy expansion only provides a quantitative improvement of the fit but at a cost of increased complexity of analysis and without affecting the main features captured by the sixth-order expansion. For instance, the trilinear coupling is found to be still dominant, with a coupling constant $\gamma_{111}^{(8th)} \approx -1.13$ eV/f.u., when the *ab initio* total energies are fitted by including up to eighth-order terms.

III. STRAIN EFFECTS

As mentioned in the introduction, substrate-induced strain is widely recognized as a major cause for the stabilization of ferroelectricity in hafnia [10,14,21,22]. Here we investigate whether such an energetically favorable dependence on strain emerges in the depicted framework, when analyzing the symmetry-allowed distortions. We recall that the growth of HfO_2 is possible on a variety of substrates (e.g., GdScO_3 , TiN , Si), resulting in different growth relationships. In particular, being dependent on the nature of the substrate surface and on the growth procedure, the direction of growth can sometimes be far from trivial. In the depicted framework, rather than focusing on a specific growth relationship, we therefore take a more general approach and analyze the effects of a set of elementary strains applied to the primitive cell. Specifically, we analyze the case of volume-conserving normal strain directed along the orthorhombic primitive vectors for six strain values $\epsilon: -3, -2, -1, 0, 1, \text{ and } 3\%$. We note that the combination of these simpler cases allows one to deduce how strain influences the hafnia stability, even when directed along nontrivial directions. Due to the *Pca2*₁ orthorhombic symmetry, the strain affects the distortion modes in different ways depending on

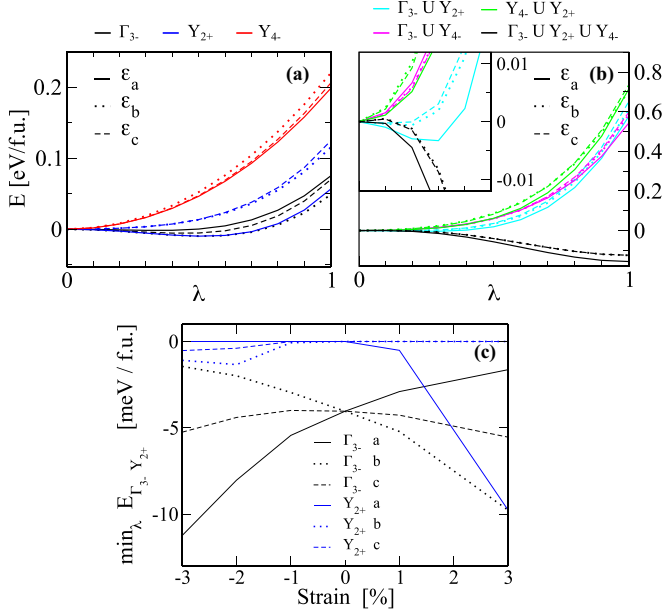


FIG. 4. (a), (b) *Ab initio* energies (in eV/f.u.) of the single symmetry-distortion modes (a), along with their couplings (b), as a function of the generalized distortion coordinate λ , when a 3% tensile strain is applied along a . The inset in panel (b) reports a zoom of the energies for λ in $[0.0, 0.5]$. The colors choice follows the one in Fig. 2: Γ_{3-} in black, Y_{2+} in blue, Y_{4-} in red (a); $\Gamma_{3-} \cup Y_{2+}$ in light blue, $\Gamma_{3-} \cup Y_{4-}$ and $\Gamma_{3-} \cup Y_{4-}$ in purple, and $Y_{2+} \cup Y_{4-}$ in green (b). The excitation of the three modes is shown in black in panel (b). Each path consists of ten intermediate structures. (c) The dependence of energy minima of the modes Γ_{3-} , in black, and Y_{2+} , in blue, on the applied strain. In each panel, the application direction is represented by a different line style.

the direction of application. As such, each ϵ has to be applied along each primitive vector.

A. Uniaxial strain effects

Let us first consider the evolution of the single modes. We refer to panel (a) of Fig. 4 for an example of the effects of a 3% tensile strain acting along the different Cartesian directions on the single modes. Each color corresponds to a different mode and each line style refers to a different application direction. The *ab initio* total energies computed along the distortions reveal how the polar mode Γ_{3-} and the pseudorotation Y_{4-} maintain their character (i.e., soft and hard, respectively) independently of the applied ϵ . The only response is a variation of the mode softness or hardness with a different strain modulus and direction of application. The effects on the second pseudorotation, instead, are more complex, as can be seen from panel (c) of Fig. 4, where the dependence of the Y_{2+} energy minimum on ϵ is reported. The trend of the Γ_{3-} instability is also reported as a comparison.

The Y_{2+} mode becomes unstable when tensile strain is applied along a and when compressive strain is applied along b and c , whereas the other strains do not induce a softening of the mode. The comparison between panels (a) of Figs. 2 and 4 gives an example of the evolution of Y_{2+} for the specific case of 3% tensile strain applied along a . A negative ϵ directed

TABLE II. Difference in total energy Δ between the $Ccce$ and the $Pca2_1$ structures, when a strain ϵ is applied along a , b , c .

ϵ (%)	Δ_a (eV/f.u.)	Δ_b (eV/f.u.)	Δ_c (eV/f.u.)
-3	-0.113	-0.152	-0.143
-2	-0.115	-0.141	-0.136
-1	-0.120	-0.132	-0.130
0	-0.126	-0.126	-0.126
1	-0.135	-0.123	-0.124
3	-0.156	-0.125	-0.125

along b and c induces a very weak instability in the pseudorotation, as shown by the shallow minimum of the *ab initio* energy profile (i.e., below 5 meV/f.u.). On the other hand, the instability is strongly enhanced by positive a -directed strain: the energy gain ≈ 0.039 eV/f.u. is comparable with the one of the polar mode when tensile strain is applied along b . Thus, essentially Y_{2+} becomes an extra soft mode under certain conditions. The evolution of this pseudorotation under external mechanical actions is strongly asymmetric with respect to the sign of the strain. Such an uneven response is not specific to the Y_{2+} mode, but it is common to the polar mode, with some differences though. Indeed, asymmetric trends in the Γ_{3-} energy profile are only detected along a - and b -directed strain; on the other hand, a c -directed strain tends to lower the energy minimum, in both compressive and tensile cases, resulting in a symmetric profile. Moreover, Γ_{3-} remains unstable under all the considered strain conditions, as confirmed by the finite energy minima. The strong dependence of Y_{2+} on strain shows how an external mechanical action could give rise to nontrivial transformation of the single modes. Nonetheless, the action of strain does not change the need for a combination of the three single modes to complete the transition to the ferroelectric phase. Panel (b) of Fig. 4 reports the effects of tensile 3% strain on the distortion coupling. Specifically, none of the combinations of two single modes is capable of driving the parent structure towards the $Pca2_1$. Indeed, the hybrid polar mode stemming from the coupling of the pseudorotations retains its stable character for all the considered strains, independently of the application direction. This is also the case for the $Y_{4-} \cup \Gamma_{3-}$ coupling, where the softness of the strained polar mode does not balance the hardness of the Y_{4-} rotation. Instead, strain destabilizes the combination $Y_{2+} \cup \Gamma_{3-}$, as can be seen in the inset of panel (b) in Fig. 4. The largest instability arises for a -directed tensile strain at its highest value considered: $\lesssim 3.5$ meV/f.u.. The other strain combinations either give rise to smaller minima or do not change the character of the combined distortion at all. Despite the insurgence of these instabilities, the coupling $Y_{2+} \cup \Gamma_{3-}$ cannot guide the transition, as shown in panel (b) of Fig. 4. Instead, as it was the case for the unstrained system, the simultaneous activation of the three distortions is required to reach the ferroelectric phase.

Table II reports the total-energy difference Δ between the $Ccce$ and the $Pca2_1$ for the different strain states. The polar phase becomes progressively more stable as tensile strain increases along the a direction. Instead, it gains stability for increasing compressive strain when applied along

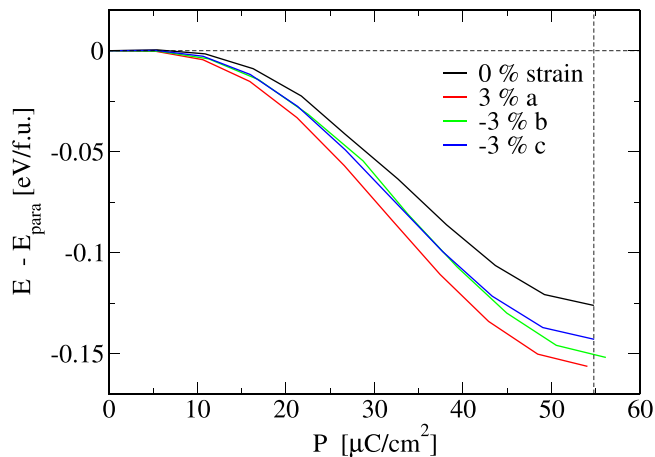


FIG. 5. Difference in *ab initio* energies between the *Ccce* and the *Pca2₁* as a function of the total polarization along the distortion. Only the trends for the most favorable strain states reported in Table II are shown.

b and *c*. Since the applied strain is volume conserving, compressive strain along *b* and *c* corresponds to an expansion along *a*. Thus, we infer that, in order to further stabilize the ferroelectric transition, an experimental strain state should involve the stretching of the *a* primitive vector from its minimum-enthalpy value. However, the stabilization connected to strain effects may come, in some cases, with a loss in the electric polarization. Indeed, Fig. 5 reports the relation between the difference in total energy between the paraelectric and the polar phase and the electric polarization arising along the distortion from the *Ccce* to the *Pca2₁* phase. We report only the most favorable strain states from Table II: each strain condition further stabilizes the transition with respect to the nonstrained case (black line). The comparison of the ferroelectric phase polarization under different strain conditions shows how the enhanced stability corresponds to a slight variation of the electric polarization. This is the case of tensile strain applied along *a* where the polarization becomes $54.07 \mu\text{C}/\text{cm}^2$, to be compared with its value $54.78 \mu\text{C}/\text{cm}^2$ under zero strain applied (vertical dashed black line). Instead, compressive strain along *b* and *c* corresponds to a slight increase to 56.14 and $54.83 \mu\text{C}/\text{cm}^2$, respectively.

In order to further investigate how strain affects different terms in the Landau free energy, we extract the parameters describing the free-energy landscape surrounding the high-symmetry *Ccce* under different strain states. The comparison of the extracted coefficients shows that the relative weight of the different terms in defining the Landau-energy profile does not change as the strain varies, at least for the four largest (in absolute value) coefficients. Instead, the relative intensity of the remaining coefficients depends on the applied strain. Figure 6 reports the trend of γ_{111} , ϵ_{131} , and ϵ_{113} with the errors of the fit as a function of the applied strain. In each panel, the continuous, dotted, and dashed lines represent *a*-directed, *b*-directed, and *c*-directed strain, respectively; the Landau coefficients are given in eV/f.u. The top panel represents the trend of ϵ_{113} . The parameter shows a clear drop—increasing its absolute value—upon increasing the strain along *a*, whereas the opposite trend is observed

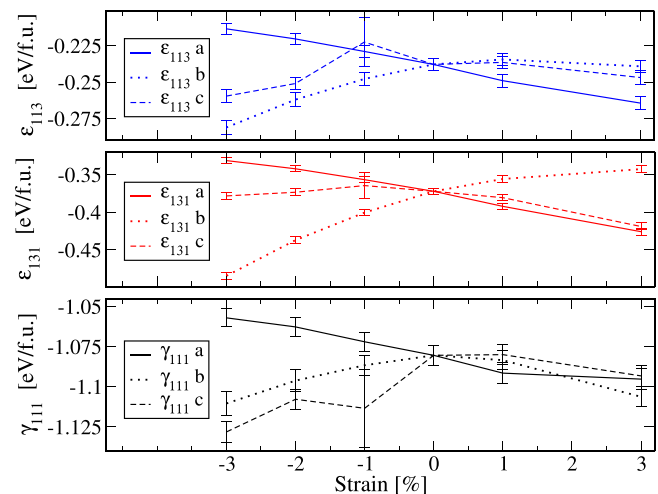


FIG. 6. Strain dependence of the three leading coefficients in Eq. (1). Top, middle, and lower panels show the ϵ_{113} , ϵ_{131} , and γ_{111} coefficients, respectively. The application directions of the strain are represented by different line styles (see legend).

increasing strain values up to the zero-strain condition along *c* and *b*. A further increase of strain along these directions corresponds to a rather flat behavior of the parameter. The middle panel shows the trend of ϵ_{131} . When increasing the strain along *a* and *c* the parameter changes towards larger negative values, whereas increasing the strain along *b* from compressive to tensile corresponds to a significant energy increase $\gtrsim 0.1$ eV/f.u. Even with the significant changes experienced by ϵ_{131} and ϵ_{113} under certain strain conditions, γ_{111} remains the largest (in absolute value) parameter for any considered strain by at least 0.5 eV/f.u. Thus γ_{111} remains the parameter leading the transition in any analyzed configuration. As reported in the bottom panel of Fig. 6, negative and positive strains along *a*, respectively, increase and decrease the trilinear coefficient with respect to its value at zero strain. Instead, *b*- and *c*-directed strains produce almost symmetric effects for compressive and tensile, corresponding in both cases to an energy gain with respect to the zero strain condition. The fourth three-mode coupling parameter ϵ_{311} is almost equivalent in value and trend to ϵ_{113} and it is therefore not shown. It is worth noticing that, in agreement with the change in character of the Y_{2+} rotation, the only parameter changing sign when moving from compressive to tensile strain is $\beta_{Y_{2+}}$, whereas the other second-order coefficients retain their sign. Also, the corresponding fourth-order parameters keep their sign fixed: specifically $\delta_{Y_{2+}}$ remains positive.

B. Experimental strain

We can now combine the effects of the considered elementary strains to reproduce an experimentally relevant configuration. The strain state of the film originates from the local lattice mismatch and relative orientation of the film with respect to the substrate. In the case of hafnia, the relative orientation is complicated by nontrivial growth directions. Accordingly, the strain applied to the primitive cell of hafnia will not be directed along its primitive lattice vectors. We focus here on HfO_2 grown on LaSrMnO_3 substrate, which

has been reported to allow for the deposition of high-quality monocrystalline films [21,23]. Specifically we focus on the work of Estandia *et al.* [22], where domain matching epitaxy (DME) is recognized as the growth mechanism of HfO_2 [111] on LaSrMnO [001]. DME allows one to accommodate high strains given by the large misfit between the substrate and the film, through the formation of local domains separated by dislocation planes detectable by x-ray diffraction (XRD). The presence of the domains allows one to introduce an effective strain f^* representing the average strain acting inside the film domain as

$$f^* = (nd_{\text{LSMO}} - md_{\text{HfO}_2})/(nd_{\text{HfO}_2}) \quad (2)$$

where d_{LSMO} and d_{HfO_2} are the lattice constant of the substrate and of the film, respectively, while n and m are the number of film planes and of substrate planes, respectively, forming the (m, n) domain. The DME mechanism allows for the minimization of f^* through the formation of different domains along the heterostructure interface. Through XRD and STEM measurements, Estandia *et al.* recognize four possible orientations of the hafnia supercell equivalent to, e.g., the one defined by the relations $[-211]_{\text{HfO}_2} \parallel [110]_{\text{LSMO}}$ and $[0-22]_{\text{HfO}_2} \parallel [-110]_{\text{LSMO}}$. The domains appearing most frequently along this orientation are (9,10) and (3,2), respectively, along $[-211]_{\text{HfO}_2}$ and $[0-22]_{\text{HfO}_2}$. Hereafter we focus on this specific combination. We decompose the strain state experienced by this domain on volume-conserving normal strains applied to the HfO_2 primitive cell, named $\boldsymbol{\varepsilon}_a$, $\boldsymbol{\varepsilon}_b$, $\boldsymbol{\varepsilon}_c$. To this end, we convert the tensors representing these strains to the experimental basis set identified by the Miller indices $\{[-2, 1, 1], [0, -2, 2], [1, 1, 1]\}$, and we look for a combination of the elementary strains $\boldsymbol{\varepsilon}'_a$, $\boldsymbol{\varepsilon}'_b$, $\boldsymbol{\varepsilon}'_c$ to reproduce the stress state identified by Estandia *et al.* (see Appendix B for the detailed derivation). According to Estandia *et al.* the HfO_2 domain (9,10)-(3,2) strain state is defined by the following conditions:

$$\varepsilon'_x = 0.03\%, \quad \varepsilon'_y = 5.3\%, \quad \sigma'_{xy} = 0\%. \quad (3)$$

where $\hat{x} = [-2, 1, 1]$, $\hat{y} = [0, -2, 2]$, and $\hat{z} = [1, 1, 1]$. Combining the three volume-conserving normal strains written in the experimental reference frame [Eq. (B4)] as $\boldsymbol{\varepsilon}' = \boldsymbol{\varepsilon}'_a - \boldsymbol{\varepsilon}'_b - \boldsymbol{\varepsilon}'_c$, we obtain a tensor $\boldsymbol{\varepsilon}'$ that respects the conditions expressed in Eq. (3). Indeed, the third condition reduces to $\varepsilon_b = \varepsilon_c$; by approximating the first condition to $\varepsilon'_x \approx 0$, we obtain $\varepsilon_a = -\varepsilon_b$. The ‘‘experimental’’ strain tensor therefore becomes

$$\boldsymbol{\varepsilon}' = \begin{pmatrix} 0 & 0 & -\frac{2}{\sqrt{2}}\varepsilon_b \\ 0 & -\frac{3}{2}\varepsilon_b & 0 \\ -\frac{2}{\sqrt{2}}\varepsilon_b & 0 & 0 \end{pmatrix}. \quad (4)$$

Thus we found a combination of elementary strains applied to the primitive cell which corresponds to the experimental strain state. Furthermore, in the context of a symmetry-distortion mode analysis, we can show how this combination corresponds to a decrease of the Landau free energy with respect to the zero-strain condition. From the first and the second conditions in Eq. (3) we know that $\varepsilon'_x \approx 0$ and $\varepsilon'_y > 0$. Thus, $\varepsilon_a > 0$ and $\varepsilon_b, \varepsilon_c < 0$. Since $\varepsilon'_y = 5.3\%$ we find $\varepsilon_b = \varepsilon_c = -3.53\%$

and $\varepsilon_a = 3.53\%$. By comparing these results with Fig. 6, we recognize how the detected elementary strain combination lowers the leading coefficients of the free energy with respect to the unstrained case. This condition corresponds to a further stabilization of the ferroelectric $Pca2_1$ phase with respect to the paraelectric phase. We stress that this decomposition only applies to the specific strain state reported for the domain detected most frequently in Ref. [22]. As such, our simplified analysis has only the intent of showing how it is possible to analyze the role of the substrate on the enhanced stability of the HfO_2 ferroelectric phase.

IV. CONCLUSIONS

In this paper we addressed the nature of the ferroelectric transition of HfO_2 through an analysis of the symmetry-allowed distortion connecting the tetragonal high-symmetry phase to the polar orthorhombic phase. We emphasize the need for the simultaneous activation of three distortion modes in order to achieve the polar phase. The first distortion Γ_{3-} is a polar unstable mode at the zone center, whereas the other two, Y_{2+} and Y_{4-} , are hard modes having a nonpolar and antipolar character, respectively. The two hard modes become polar only when considered as coupled, giving rise to a hybrid mode that, however, retains its hard character. The term dominating the Landau free-energy expansion is the trilinear coupling, with the fifth-order terms acting as higher-order corrections. The lack of a clear leading order parameter raises the question on whether the energetics is affected by different factors, such as different growth conditions. For this reason we analyzed how the strain affects the depicted framework. Our results show that the need for the coupling of the three modes remains unaltered, independently of the specific external mechanical action. The complex dependence on strain appears in the change of nature of the Y_{2+} mode, which becomes unstable under certain conditions. Nonetheless, as for Γ_{3-} , this instability cannot induce the complete transition by itself. The fit of the free energy strengthens the idea that the simultaneous excitation of the three modes, along with their coupling, is necessary for the full transition to occur. Finally, we applied this framework to the realistic case of HfO_2 grown on LaSrMnO_3 . This configuration is complicated by DME, proposed in the context of an epitaxial film subjected to a uniform strain. We considered the domain experimentally detected most frequently by Estandia *et al.* [22], but even in this case our analysis on the effect of the strain f^* is valid only locally. Nonetheless, though applied with a heuristic approach, the strain decomposition confirms the existence of strain states that favor the transition towards a ferroelectric phase, along with some others that penalize it. The aim of our analysis here is not to give an exhaustive explanation for the mechanism underlying the ferroelectric transition in HfO_2 , but is rather meant as a first step towards a general microscopic description of the effect. Further steps in this direction will be the analysis of the single-mode features to detect the microscopic origin of the energy gain of their trilinear coupling, along with the relative stability of the monoclinic vs orthorhombic phases in strained film bulk performed through symmetry mode analysis, issues which we leave for future works.

ACKNOWLEDGMENTS

We acknowledge support from the Italian Ministry for Research and Education through the Progetto di Rilevante Interesse Nazionale (PRIN)-2017 Project “*TWEET: Towards Ferroelectricity in Two dimensions*” (IT-Ministero dell’Istruzione e ministero dell’Università e Ricerca (MIUR) Grant No. 2017YCTB59) and computational support from Consorzio INteruniversitario pEr il Calcolo Automatico (CINECA) through the IS CRA initiative under Grant No. HP10CSYH10 (TWEET Project). We also acknowledge support from the computational resources at “Gabriele d’Annunzio” University of Chieti.

APPENDIX A: COMPUTATIONAL DETAILS

Density functional theory simulations were performed using the Vienna Ab-Initio Simulation Package (VASP) [44]. We relaxed the orthorhombic primitive cell within the revised Perdew, Burke, and Ernzerhof functional for solids [45,46] until total-energy change between two successive self-consistent steps is smaller than 10^{-7} eV and forces are smaller than 10^{-3} eV/Å. The cutoff for the expansion onto the plane-wave basis is set to 400 eV. As for the distortion mode analysis, we compute the energy of structures along the distortion paths, with the PBEsol functional and a k -point density of $\approx 4.5 \times 10^3$ points Å³. The strain is included applying the volume-conservative deformations reported in Eq. (B3) to the orthorhombic primitive cell. We stress that these trans-

formations consist in pure normal strains: the orthorhombic symmetry is thus preserved. Once the primitive cell is deformed, the internal coordinates are relaxed until the forces are smaller than 10^{-3} eV/Å. The distortion paths employed to perform the fits under different strain conditions are built from these relaxed configurations. The symmetry-distortion analysis summarized in Fig. 1 is repeated for each different considered strain. The electric polarization is computed through the Berry-phase method [47–49] as implemented in VASP.

APPENDIX B: STRAIN

The change from the basis identified by the Miller indices $\{[1, 0, 0], [0, 1, 0], [0, 0, 1]\}$ (where we performed the simulations) to the one identified by $\{[-2, 1, 1], [0, -2, 2], [1, 1, 1]\}$ is obtained through the transformation

$$\boldsymbol{\varepsilon}' = \mathbf{Q}^T \boldsymbol{\varepsilon} \mathbf{Q}$$

where \mathbf{Q} is the direction-cosine matrix and \mathbf{Q}^T is its transpose. Thus $\mathbf{Q}_{i,j} = \hat{\varepsilon}'_i \cdot \hat{\varepsilon}_j$ where $\hat{\varepsilon}'_i$ is a vector of the supercell basis, and $\hat{\varepsilon}_j$ is a vector of the primitive cell basis both normalized to unity. The \mathbf{Q} matrix is

$$\mathbf{Q} = \begin{pmatrix} -2/\sqrt{6} & 1/\sqrt{6} & 1/\sqrt{6} \\ 0 & -1/\sqrt{2} & 1/\sqrt{2} \\ 1/\sqrt{3} & 1/\sqrt{3} & 1/\sqrt{3} \end{pmatrix}. \quad (\text{B1})$$

Since $\boldsymbol{\varepsilon}$ is diagonal, the strain matrix in the “experimental” reference frame will be

$$\boldsymbol{\varepsilon}' = \begin{pmatrix} \frac{1}{6}(4\epsilon_a + \epsilon_b + \epsilon_c) & \frac{1}{\sqrt{12}}(-\epsilon_b + \epsilon_c) & \frac{1}{\sqrt{18}}(-2\epsilon_a + \epsilon_b + \epsilon_c) \\ \frac{1}{\sqrt{12}}(-\epsilon_b + \epsilon_c) & \frac{1}{2}(\epsilon_b + \epsilon_c) & \frac{1}{\sqrt{6}}(-\epsilon_b + \epsilon_c) \\ \frac{1}{\sqrt{18}}(-2\epsilon_a + \epsilon_b + \epsilon_c) & \frac{1}{\sqrt{6}}(-\epsilon_b + \epsilon_c) & \frac{1}{3}(\epsilon_a + \epsilon_b + \epsilon_c) \end{pmatrix}. \quad (\text{B2})$$

Consider now, for instance, a volume-conserving normal strain ϵ_a directed along the primitive vector a ; the primitive vectors transform as

$$\begin{aligned} a &= a_0(1 + \epsilon_a), \\ b &= b_0/\sqrt{1 + \epsilon_a}, \\ c &= c_0/\sqrt{1 + \epsilon_a}. \end{aligned} \quad (\text{B3})$$

In the limit of small ϵ_a the strain tensor reads

$$\boldsymbol{\varepsilon}_{\mathbf{a}} = \begin{pmatrix} \epsilon_a & 0 & 0 \\ 0 & -\epsilon_a/2 & 0 \\ 0 & 0 & -\epsilon_a/2 \end{pmatrix}$$

where “small strains” refers to values up to $\approx 5\%$ for which the discrepancy between $1/(\sqrt{1 + \epsilon})$ and $1 - \epsilon/2$ is $\approx 0.1\%$.

The tensors for strains along b and c are analogous. These three strains when acting independently are written in the experimental frame of reference as

$$\begin{aligned} \boldsymbol{\varepsilon}'_{\mathbf{a}} &= \begin{pmatrix} \epsilon_a/2 & 0 & \epsilon_a/\sqrt{2} \\ 0 & -\epsilon_a & 0 \\ \epsilon_a/\sqrt{2} & 0 & 0 \end{pmatrix}, \\ \boldsymbol{\varepsilon}'_{\mathbf{b}} &= \begin{pmatrix} -\epsilon_b/4 & -\sqrt{3}\epsilon_b/4 & \epsilon_b/2\sqrt{2} \\ -\epsilon_b/2\sqrt{2} & \epsilon_b/4 & -3\epsilon_b/2\sqrt{6} \\ \epsilon_b/2\sqrt{2} & -3\epsilon_b/2\sqrt{6} & 0 \end{pmatrix}, \\ \boldsymbol{\varepsilon}'_{\mathbf{c}} &= \begin{pmatrix} -\epsilon_c/4 & \sqrt{3}\epsilon_c/4 & \epsilon_c/2\sqrt{2} \\ \epsilon_c/2\sqrt{2} & \epsilon_c/4 & 3\epsilon_c/2\sqrt{6} \\ \epsilon_c/2\sqrt{2} & 3\epsilon_c/2\sqrt{6} & 0 \end{pmatrix}. \end{aligned} \quad (\text{B4})$$

The combination $\boldsymbol{\varepsilon}' = \boldsymbol{\varepsilon}'_{\mathbf{a}} - \boldsymbol{\varepsilon}'_{\mathbf{b}} - \boldsymbol{\varepsilon}'_{\mathbf{c}}$ results in

$$\boldsymbol{\varepsilon}' = \begin{pmatrix} -\frac{1}{4}(2\epsilon_a + \epsilon_b + \epsilon_c) & \frac{\sqrt{3}\epsilon}{4}(-\epsilon_b + \epsilon_c) & \frac{1}{2\sqrt{2}}(2\epsilon_a - \epsilon_b - \epsilon_c) \\ \frac{\sqrt{3}\epsilon}{4}(-\epsilon_b + \epsilon_c) & \frac{1}{4}(4\epsilon_a - \epsilon_b - \epsilon_c) & \frac{3}{2\sqrt{6}}(\epsilon_b - \epsilon_c) \\ \frac{1}{2\sqrt{2}}(2\epsilon_a - \epsilon_b - \epsilon_c) & \frac{3}{2\sqrt{6}}(\epsilon_b - \epsilon_c) & 0 \end{pmatrix}, \quad (\text{B5})$$

which can be adapted to represent the experimentally detected strain state. Notice that there exists a combination that would lead to a diagonal tensor $\boldsymbol{\varepsilon}'$, which is $\epsilon_b = \epsilon_c = \epsilon_a$. But in such case we find $\varepsilon'_x = \epsilon_a$ and $\varepsilon'_y = \epsilon_a/2$, which cannot reproduce the conditions in Eq. (3).

- [1] Y. S. Lin, R. Puthenkovilakam, and J. P. Chang, Dielectric property and thermal stability of HfO₂ on silicon, *Appl. Phys. Lett.* **81**, 2041 (2002).
- [2] G. D. Wilk, R. M. Wallace, and J. M. Anthony, Hafnium and zirconium silicates for advanced gate dielectrics, *J. Appl. Phys.* **87**, 484 (2000).
- [3] H. Zhu, C. Tang, L. Fonseca, and R. Ramprasad, Recent progress in *ab initio* simulations of hafnia-based gate stacks, *J. Mater. Sci.* **47**, 7399 (2012).
- [4] J. Robertson, High dielectric constant gate oxides for metal oxide Si transistors, *Rep. Prog. Phys.* **69**, 327 (2005).
- [5] T. S. Börscke, J. Müller, D. Bräuhaus, U. Schröder, and U. Böttger, Ferroelectricity in hafnium oxide thin films, *Appl. Phys. Lett.* **99**, 102903 (2011).
- [6] T. S. Börscke, J. Müller, D. Bräuhaus, U. Schröder, and U. Böttger, Ferroelectricity in hafnium oxide: CMOS compatible ferroelectric field effect transistors, in *Proceedings of the 2011 International Electron Devices Meeting* (IEEE, Piscataway, NJ, 2011), pp. 24.5.1–24.5.4.
- [7] T. Mikolajick, S. Slesazeck, M. H. Park, and U. Schröder, Ferroelectric hafnium oxide for ferroelectric random-access memories and ferroelectric field-effect transistors, *MRS Bull.* **43**, 340 (2018).
- [8] Y. Wei, S. Matzen, T. Maroutian, G. Agnus, M. Salverda, P. Nukala, Q. Chen, J. Ye, P. Lecoeur, and B. Noheda, Magnetic Tunnel Junctions Based on Ferroelectric Hf_{0.5}Zr_{0.5}O₂ Tunnel Barriers, *Phys. Rev. Appl.* **12**, 031001(R) (2019).
- [9] S. Barabash, Prediction of new metastable HfO₂ phases: toward understanding ferro- and antiferroelectric films, *J. Comput. Electron.* **16**, 1227 (2017).
- [10] Y. Wei, P. Nukala, M. Salverda, S. Matzen, H. J. Zhao, J. Momand, A. S. Everhardt, G. Agnus, G. R. Blake, P. Lecoeur *et al.*, A rhombohedral ferroelectric phase in epitaxially strained Hf_{0.5}Zr_{0.5}O₂ thin films, *Nat. Mater.* **17**, 1095 (2018).
- [11] Y. Qi, S. Singh, C. Lau, F. T. Huang, X. Xu, F. J. Walker, C. H. Ahn, S. W. Cheong, and K. M. Rabe, Stabilization of Competing Ferroelectric Phases of HfO₂ under Epitaxial Strain, *Phys. Rev. Lett.* **125**, 257603 (2020).
- [12] T. D. Huan, V. Sharma, G. A. Rossetti, and R. Ramprasad, Pathways towards ferroelectricity in hafnia, *Phys. Rev. B* **90**, 064111 (2014).
- [13] X. Xu, F.-T. Huang, Y. Qi, S. Singh, K. M. Rabe, D. Obeyseker, J. Yang, M.-W. Chu, and S.-W. Cheong, Kinetically-stabilized ferroelectricity in bulk single-crystalline HfO₂:Y, *Nat. Mater.* **20**, 826 (2021).
- [14] Y. Zhang, Q. Yang, L. Tao, E. Y. Tsybal, and V. Alexandrov, Effects of Strain and Film Thickness on the Stability of the Rhombohedral Phase of Hf_{0.5}Zr_{0.5}O₂, *Phys. Rev. Appl.* **14**, 014068 (2020).
- [15] E. Yurchuk, J. Müller, S. Knebel, J. Sundqvist, A. P. Graham, T. Melde, U. Schröder, and T. Mikolajick, Impact of layer thickness on the ferroelectric behaviour of silicon doped hafnium oxide thin films, *Thin Solid Films* **533**, 88 (2013).
- [16] H. J. Lee, M. Lee, K. Lee, J. Jo, H. Yang, Y. Kim, S. C. Chae, U. Waghmare, and J. H. Lee, Scale-free ferroelectricity induced by flat phonon bands in HfO₂, *Science* **369**, 1343 (2020).
- [17] J. Junquera and P. Ghosez, Critical thickness for ferroelectricity in perovskite ultrathin films, *Nature (London)* **422**, 506 (2003).
- [18] I. P. Batra, P. Wurfel, and B. D. Silverman, Phase transition, stability, and depolarization field in ferroelectric thin films, *Phys. Rev. B* **8**, 3257 (1973).
- [19] T. P. Ma and J.-P. Han, Why is nonvolatile ferroelectric memory field-effect transistor still elusive?, *IEEE Electron Device Lett.* **23**, 386 (2002).
- [20] M. Dawber, K. M. Rabe, and J. F. Scott, Physics of thin-film ferroelectric oxides, *Rev. Mod. Phys.* **77**, 1083 (2005).
- [21] S. Estandia, N. Dix, J. Gazquez, I. Fina, J. Lyu, M. F. Chisholm, J. Fontcuberta, and F. Sánchez, Engineering ferroelectric Hf_{0.5}Zr_{0.5}O₂ thin films by epitaxial stress, *ACS Appl. Electron. Mater.* **1**, 1449 (2019).
- [22] S. Estandia, N. Dix, M. F. Chisholm, I. Fina, and F. Sánchez, Domain-matching epitaxy of ferroelectric Hf_{0.5}Zr_{0.5}O₂(111) on La_{2/3}Sr_{1/3}MnO₃(001), *Cryst. Growth Des.* **20**, 3801 (2020).
- [23] P. Nukala, J. Antoja-Lleonart, Y. Wei, L. Yedra, B. Dkhil, and B. Noheda, Direct epitaxial growth of polar (1-x)HfO₂-(x)ZrO₂ ultrathin films on silicon, *ACS Appl. Electron. Mater.* **1**, 2585 (2019).
- [24] J. Müller, T. S. Börscke, U. Schröder, U. Böttger, and T. Mikolajick, Ferroelectricity in simple binary ZrO₂ and HfO₂, *Nano Lett.* **12**, 4318 (2012).
- [25] E. D. Grimley, T. Schenk, T. Mikolajick, U. Schröder, and J. M. LeBeau, Atomic structure of domain and interphase boundaries in ferroelectric HfO₂, *Adv. Mater. Interfaces* **5**, 1701258 (2018).
- [26] R. Batra, T. D. Huan, J. L. Jones, G. Rossetti, and R. Ramprasad, Factors favoring ferroelectricity in hafnia: A first-principles computational study, *J. Phys. Chem. C* **121**, 4139 (2017).
- [27] U. Schröder, C. Richter, M. H. Park, T. Schenk, M. Pesić, M. Hoffmann, F. P. G. Fengler, D. Pohl, B. Rellinghaus, C. Zhou *et al.*, Lanthanum-doped hafnium oxide: A robust ferroelectric material, *Inorg. Chem.* **57**, 2752 (2018).
- [28] M. Hoffmann, U. Schröder, T. Schenk, T. Shimizu, H. Funakubo, O. Sakata, D. Pohl, M. Drescher, C. Adelman, R. Materlik *et al.*, Stabilizing the ferroelectric phase in doped hafnium oxide, *J. Appl. Phys.* **118**, 072006 (2015).
- [29] P. Polakowski and J. Müller, Ferroelectricity in undoped hafnium oxide, *Appl. Phys. Lett.* **106**, 232905 (2015).
- [30] S. Liu and B. M. Hanrahan, Effects of growth orientations and epitaxial strains on phase stability of HfO₂ thin films, *Phys. Rev. Material* **3**, 054404 (2019).
- [31] H. T. Stokes, D. M. Hatch, B. J. Campbell, and D. E. Tanner, ISODISPLACE: A web-based tool for exploring structural distortions, *J. Appl. Cryst.* **39**, 607 (2006).
- [32] H. T. Stokes, S. V. Orden, and B. J. Campbell, ISOSUBGROUP: An internet tool for generating isotropy subgroups of crystallographic space groups, *J. Appl. Cryst.* **49**, 1849 (2016).
- [33] D. Orobengoa, C. Capillas, M. I. Aroyo, and J. M. Perez-Mato, AMPLIMODES: Symmetry-mode analysis on the Bilbao Crystallographic Server, *J. Appl. Cryst.* **42**, 820 (2009).
- [34] J. M. Perez-Mato, D. Orobengoa, and M. I. Aroyo, Mode crystallography of distorted structures, *Acta Cryst. A* **66**, 558 (2010).
- [35] H. T. Stokes and D. M. Hatch, FINDSYM: Program for identifying the space-group symmetry of a crystal, *J. Appl. Cryst.* **38**, 237 (2005).
- [36] H. T. Stokes, D. M. Hatch, and B. J. Campbell, FINDSYM, ISOTROPY Software Suite, <https://stokes.byu.edu/iso/findsym.php>.

- [37] E. Bousquet, M. Dawber, N. Stucki, C. Lichtensteiger, P. Hermet, S. Gariglio, J.-M. Triscone, and P. Ghosez, Improper ferroelectricity in perovskite oxide artificial superlattices, *Nature (London)* **452**, 732 (2008).
- [38] N. A. Benedek and C. J. Fennie, Hybrid Improper Ferroelectricity: A Mechanism for Controllable Polarization-Magnetization Coupling, *Phys. Rev. Lett.* **106**, 107204 (2011).
- [39] A. Stroppa, P. Barone, P. Jain, J. M. Perez-Mato, and S. Picozzi, Hybrid improper ferroelectricity in a multiferroic and magneto-electric metal-organic framework, *Adv. Mater.* **25**, 2284 (2013).
- [40] H. J. Zhao, J. Íñiguez, W. Ren, X. M. Chen, and L. Bellaiche, Atomistic theory of hybrid improper ferroelectricity in perovskites, *Phys. Rev. B* **89**, 174101 (2014).
- [41] M. Stengel, C. J. Fennie, and Ph. Ghosez, Electrical properties of improper ferroelectrics from first principles, *Phys. Rev. B* **86**, 094112 (2012).
- [42] I. Etxebarria, J. M. Perez-Mato, and P. Boullay, The role of trilinear couplings in the phase transitions of Aurivillius compounds, *Ferroelectrics* **401**, 17 (2010).
- [43] V. K. Wadhavan, *Introduction to Ferroic Materials* (CRC, Boca Raton, FL, 2000).
- [44] G. Kresse and D. Joubert, From ultrasoft pseudopotentials to the projector augmented-wave method, *Phys. Rev. B* **59**, 1758 (1999).
- [45] J. P. Perdew, A. Ruzsinszky, G. I. Csonka, O. A. Vydrov, G. E. Scuseria, L. A. Constantin, X. Zhou, and K. Burke, Restoring the Density-Gradient Expansion for Exchange in Solids and Surfaces, *Phys. Rev. Lett.* **100**, 136406 (2008).
- [46] G. I. Csonka, J. P. Perdew, A. Ruzsinszky, P. H. T. Philipsen, S. Lebègue, J. Paier, O. A. Vydrov, and J. G. Ángyán, Assessing the performance of recent density functionals for bulk solids, *Phys. Rev. B* **79**, 155107 (2009).
- [47] R. D. King-Smith and D. Vanderbilt, Theory of polarization of crystalline solids, *Phys. Rev. B* **47**, 1651 (1993).
- [48] R. Resta, Macroscopic polarization in crystalline dielectrics: The geometric phase approach, *Rev. Mod. Phys.* **66**, 899 (1994).
- [49] N. A. Spaldin, A beginner's guide to the modern theory of polarization, *J. Solid State Chem.* **195**, 2 (2012).